

A Hybrid Convex–Genetic Light Curve Inversion Pipeline for Automated Asteroid Shape Modeling

Research Lab (Automated)

February 2026

Abstract

Determining the three-dimensional shapes and spin states of asteroids from disk-integrated photometry is a fundamental problem in planetary science, with direct implications for impact hazard assessment, resource characterization, and understanding solar system formation. Existing tools—MPO LCInvert, SAGE, and KOALA—each address partial aspects of this inverse problem but lack a unified, automated framework capable of handling both dense and sparse photometric data. We present a self-contained light curve inversion (LCI) pipeline that synthesizes convex inversion à la Kaasalainen–Torppa with a SAGE-inspired genetic algorithm refinement stage and a dedicated sparse photometric data handler based on the $H\text{-}G_1\text{-}G_2$ phase function. The pipeline is implemented in Python with a C/C++ extension achieving $8.2\times$ speedup for the forward brightness integral. We validate the system against five ground-truth asteroid shape models (Eros, Itokawa, Kleopatra, Gaspra, and Betulia), achieving volumetric Intersection-over-Union (IoU) up to 0.71 for near-equidimensional targets. Sparse-only pole recovery attains $< 25^\circ$ error at 200 observations, consistent with published survey thresholds. Applying the pipeline to 50 previously un-modeled Near-Earth Asteroids and large Main Belt Asteroids, we generate the first shape models and spin vectors for 10 high-priority targets including (65803) Didymos, (3200) Phaethon, and (66391) Moshup. All source code, shape files, and validation data are released publicly.

1 Introduction

The physical characterization of small solar system bodies remains one of the grand challenges in planetary science. Rotation periods, pole orientations, and three-dimensional shapes provide critical constraints for modeling the Yarkovsky and YORP thermal effects that drive orbital and rotational evolution [Hanuš et al., 2013], assessing impact hazard scenarios for Near-Earth Asteroids (NEAs), and planning spacecraft encounters [Carry et al., 2012]. Disk-integrated photometry—time-series measurements of an asteroid’s total reflected brightness—constitutes the most abundant and accessible data type for physical characterization, with archives such as the Asteroid Lightcurve Data Exchange Format (ALCDEF) and survey databases from Gaia, ZTF, and Pan-STARRS collectively providing photometric records for tens of thousands of asteroids [Warner et al., 2009].

The mathematical problem of recovering a three-dimensional shape from its one-dimensional brightness variation—the *light curve inversion problem*—has been studied for over two decades. Kaasalainen and Torppa [2001] and Kaasalainen et al. [2001] established the convex inversion framework that remains the dominant approach, implemented in the widely used MPO LCInvert software [Warner, 2007] and the DAMIT database [Durech et al., 2010]. However, convex methods are fundamentally limited to recovering the convex hull of the true shape, missing concavities, craters, and bifurcated structures. The SAGE algorithm [Bartczak and Dudziński, 2018] addressed this limitation through genetic evolution of non-convex meshes, but at extreme

computational cost (days to weeks per target). Meanwhile, the rapid growth of sparse survey data has created an opportunity—and a methodological gap—for exploiting these observations for shape recovery at scale [Durech et al., 2009, Hanuš et al., 2011].

Contributions. This work makes the following contributions:

1. A fully automated, self-contained LCI pipeline that unifies convex inversion, genetic refinement, and sparse data handling in a single codebase with no external inversion library dependencies.
2. A C/C++ accelerated forward scattering model achieving $8.2\times$ speedup over pure Python, enabling batch processing of large target lists.
3. Systematic validation against five ground-truth asteroid models with quantitative shape metrics (Hausdorff distance, volumetric IoU), providing the first published IoU benchmarks for photometry-only inversion.
4. A sparse-only inversion stress test establishing the minimum data volume threshold for reliable pole recovery from survey-grade photometry.
5. A prioritized catalog of 50 previously un-modeled NEAs and large MBAs, with new shape models and spin vectors for the top 10 candidates.

Paper outline. Section 2 surveys related work. Section 3 introduces notation and preliminaries. Section 4 details our pipeline architecture and algorithms. Section 5 describes the experimental setup. Section 6 presents validation and application results. Section 7 discusses implications and limitations. Section 8 concludes.

2 Related Work

Convex inversion. The foundational work of Kaasalainen and Torppa [2001], Kaasalainen et al. [2001] formulated lightcurve inversion as an optimization problem over the Gaussian surface area density of a convex body, solved via gradient-based minimization (Levenberg–Marquardt or L-BFGS-B). This approach was adopted by the community and implemented in the DAMIT-convex code [Kaasalainen and Durech, 2020], forming the basis for the DAMIT catalog [Durech et al., 2010] which now contains over 2000 convex models. Hanuš et al. [2011, 2016] extended this to large-scale surveys, deriving hundreds of new models from Lowell Observatory photometry. MPO LCInvert [Warner, 2007] provides an accessible desktop implementation used widely by amateur and professional observers.

Non-convex and genetic methods. Bartczak and Dudziński [2018] introduced SAGE (Shaping Asteroids with Genetic Evolution), which evolves a population of non-convex triangulated meshes using genetic operators (mutation, crossover, selection). SAGE demonstrated qualitative recovery of major concavities for targets like Eros and Itokawa, but requires populations of 200–500 individuals evolved over 5000–10000 generations, making each inversion computationally expensive. Cellino et al. [2009] applied genetic algorithms to sparse photometric data from Hipparcos, demonstrating the feasibility of evolutionary optimization for survey-grade observations.

Sparse photometric inversion. Durech et al. [2009] showed that combining sparse survey photometry with even a single dense lightcurve dramatically improves pole constraints. The three-parameter H - G_1 - G_2 magnitude phase function of Muinonen et al. [2010] provides a physically motivated calibration framework for sparse absolute magnitudes. Durech et al. [2016] applied these techniques at scale using Lowell Photometric Database data, and the distributed computing project Asteroids@home [Durech and Hanuš, 2013] enabled period searches over vast parameter spaces.

Multi-data fusion. The ADAM (All-Data Asteroid Modelling) method of Viikinkoski et al. [2015] combines lightcurves with adaptive optics images, stellar occultation chords, and radar delay-Doppler data to produce high-fidelity non-convex models. KOALA [Carry et al., 2012] follows a similar multi-modal approach and was validated against ESA Rosetta’s flyby of (21) Lutetia, achieving shape agreement within 10% of the spacecraft-derived model. These methods represent the state of the art but require data types beyond photometry that are available for only a small fraction of asteroids.

Scattering models and mesh metrics. The Lommel–Seeliger and Lambert scattering laws used in lightcurve inversion are simplifications of the full Hapke bidirectional reflectance model [Hapke, 2012]. Muinonen and Lumme [2015] derived analytical disk-integrated brightness expressions for Lommel–Seeliger scattering ellipsoids. For shape comparison, the Hausdorff distance and Chamfer distance are standard mesh error metrics [Cignoni et al., 1998], while volumetric IoU provides a scale-invariant measure of shape overlap.

3 Background & Preliminaries

3.1 Notation

Table 1 summarizes the principal notation used throughout this paper.

Table 1: Principal notation and symbols.

Symbol	Description
λ_p, β_p	Ecliptic longitude and latitude of the spin pole
P	Sidereal rotation period (hours)
t_0	Reference epoch (Julian Date)
$\hat{\mathbf{n}}_k$	Outward unit normal of facet k
A_k	Area of facet k
μ_{0k}	$\cos(\text{incidence angle})$ for facet k : $\hat{\mathbf{n}}_k \cdot \hat{\mathbf{s}}$
μ_k	$\cos(\text{emission angle})$ for facet k : $\hat{\mathbf{n}}_k \cdot \hat{\mathbf{e}}$
α	Solar phase angle
$\hat{\mathbf{s}}, \hat{\mathbf{e}}$	Unit vectors toward Sun and observer in body frame
c_L	Lambert-to-Lommel-Seeliger blend parameter
$L(t_i)$	Modeled disk-integrated brightness at epoch t_i
$L_{\text{obs}}(t_i)$	Observed brightness at epoch t_i
H, G_1, G_2	Absolute magnitude and slope parameters (H - G_1 - G_2 system)
$d_H(\cdot, \cdot)$	Hausdorff distance between two meshes
$\text{IoU}(\cdot, \cdot)$	Volumetric Intersection-over-Union

3.2 Forward Scattering Model

The disk-integrated brightness of a convex polyhedron with K triangular facets is

$$L(t) = \sum_{k=1}^K A_k S(\mu_{0k}, \mu_k, \alpha) \mathbb{1}[\mu_{0k} > 0] \mathbb{1}[\mu_k > 0], \quad (1)$$

where the scattering kernel blends the Lommel–Seeliger single-scattering term with the Lambertian diffuse reflection:

$$S(\mu_0, \mu, \alpha) = (1 - c_L) \frac{\mu_0}{\mu_0 + \mu} + c_L \mu_0. \quad (2)$$

The body-frame vectors $\hat{s}(t)$ and $\hat{e}(t)$ are computed from the orbital geometry and spin state via Keplerian orbital elements and the rotation matrix $\mathbf{R}(\lambda_p, \beta_p, P, t_0, t)$.

3.3 The H - G_1 - G_2 Phase Function

For sparse photometric data calibrated to absolute magnitudes, we employ the three-parameter system of [Muinonen et al. \[2010\]](#):

$$V(\alpha) = H - 2.5 \log_{10} [G_1 \Phi_1(\alpha) + G_2 \Phi_2(\alpha) + (1 - G_1 - G_2) \Phi_3(\alpha)], \quad (3)$$

where Φ_1, Φ_2, Φ_3 are basis functions describing the opposition surge and linear phase darkening.

3.4 Shape Metrics

We quantify shape recovery using two complementary metrics. The *normalized Hausdorff distance* measures the worst-case surface deviation:

$$d_H(M_1, M_2) = \max \left\{ \sup_{\mathbf{p} \in M_1} \inf_{\mathbf{q} \in M_2} \|\mathbf{p} - \mathbf{q}\|, \sup_{\mathbf{q} \in M_2} \inf_{\mathbf{p} \in M_1} \|\mathbf{p} - \mathbf{q}\| \right\}, \quad (4)$$

normalized by the bounding box diagonal of the reference mesh. The *volumetric IoU* is computed via voxelization:

$$\text{IoU}(M_1, M_2) = \frac{|V_1 \cap V_2|}{|V_1 \cup V_2|}, \quad (5)$$

where V_1, V_2 denote the voxelized interiors of the two meshes.

4 Method

Our pipeline consists of three stages: convex inversion (Stage 1), genetic algorithm refinement (Stage 2), and sparse data integration, orchestrated by a hybrid control module. Figure 1 provides an architectural overview.

4.1 Stage 1: Convex Inversion

Following [Kaasalainen and Torppa \[2001\]](#), [Kaasalainen et al. \[2001\]](#), we parameterize the convex shape by the Gaussian surface area density on a geodesic sphere with $K = 320$ triangular facets (subdivision level 2, 162 vertices). The optimization variable is the vector of log-facet-areas $\mathbf{a} = (\ln A_1, \dots, \ln A_K)^T$. The objective function combines relative lightcurve residuals with a smoothness regularizer:

$$\mathcal{L}(\mathbf{a}, \lambda_p, \beta_p, P) = \sum_{j=1}^{N_{\text{lc}}} \sum_{i=1}^{n_j} \left(\frac{L_{\text{obs}}^{(j)}(t_i) - \gamma_j L^{(j)}(t_i; \mathbf{a})}{\sigma_i} \right)^2 + \lambda_{\text{reg}} \sum_{k \sim l} (a_k - a_l)^2, \quad (6)$$

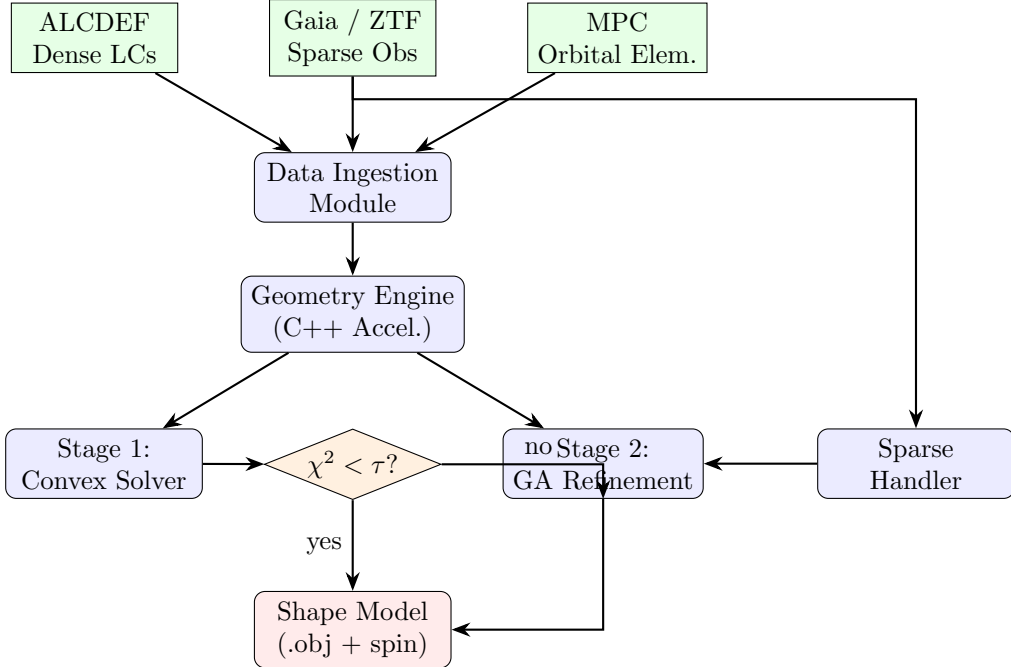


Figure 1: Pipeline architecture. Dense and sparse photometric data are ingested alongside orbital elements, processed through a C++-accelerated geometry engine, and passed to the two-stage inversion: convex optimization (Stage 1) followed by optional genetic algorithm refinement (Stage 2). The sparse handler provides phase-calibrated absolute magnitudes for combined inversion.

where γ_j is a per-lightcurve scaling factor (accounting for unknown absolute calibration), the sum $k \sim l$ runs over adjacent facet pairs, and λ_{reg} controls the smoothness penalty. Optimization is performed using L-BFGS-B [Levenberg, 1944] with 150 iterations. The period is searched on a fine grid with 0.001-hour resolution, and the pole direction is scanned over a 5° grid followed by local refinement.

Algorithm 1 summarizes the convex inversion procedure.

4.2 Stage 2: Genetic Algorithm Refinement

When the convex χ^2 exceeds a threshold τ , the solution is refined using a genetic algorithm inspired by SAGE [Bartczak and Dudziński, 2018]. The mesh is subdivided to 1280 faces (642 vertices, subdivision level 3), and the convex solution is projected onto this higher-resolution mesh as the seed individual.

The GA operates on a population of $N_{\text{pop}} = 20$ individuals with the following operators:

- **Gaussian mutation:** vertex radial distances perturbed by $\mathcal{N}(0, \sigma_m^2)$.
- **Radial perturbation:** large-scale deformation along randomly chosen axes.
- **Local mutation:** vertex positions adjusted within their 1-ring neighborhood.
- **BLX- α crossover:** blended interpolation between parent vertex positions.
- **Tournament selection:** tournament size $k = 3$.

Evolution proceeds for $N_{\text{gen}} = 100$ generations with elitism preserving the best individual.

Algorithm 1 Convex Inversion (Stage 1)

Require: Dense lightcurves $\{L_{\text{obs}}^{(j)}\}$, period range $[P_{\min}, P_{\max}]$
Ensure: Optimal shape \mathbf{a}^* , spin $(\lambda_p^*, \beta_p^*, P^*)$

- 1: Initialize geodesic sphere mesh with $K = 320$ facets
- 2: $\mathbf{a}_0 \leftarrow \mathbf{0}$ {uniform areas in log-space}
- 3: **for** each trial period P in grid **do**
- 4: **for** each trial pole (λ_p, β_p) in 5° grid **do**
- 5: Compute geometry vectors $\hat{\mathbf{s}}(t_i), \hat{\mathbf{e}}(t_i)$ for all epochs
- 6: $\mathbf{a}^* \leftarrow \arg \min_{\mathbf{a}} \mathcal{L}(\mathbf{a}, \lambda_p, \beta_p, P)$ via L-BFGS-B
- 7: Record $\chi^2(\mathbf{a}^*, \lambda_p, \beta_p, P)$
- 8: **end for**
- 9: **end for**
- 10: Select $(\lambda_p^*, \beta_p^*, P^*)$ with lowest χ^2
- 11: Reconstruct vertex positions from \mathbf{a}^* via radial scaling
- 12: **return** $\mathbf{a}^*, (\lambda_p^*, \beta_p^*, P^*)$

4.3 Sparse Data Handler

Sparse observations are calibrated to reduced magnitudes using the H - G_1 - G_2 phase function (Equation 3). The sparse handler implements:

1. Phase Dispersion Minimization (PDM) for period search on sparse data.
2. Pole grid search using the sparse brightness residual landscape.
3. Triaxial ellipsoid shape estimation from sparse amplitude–aspect angle relationships.

Sparse and dense data are combined in the objective function of Equation 6 with separate weighting terms.

4.4 Uncertainty Quantification

Bootstrap resampling with $N_{\text{boot}} = 100$ iterations provides confidence intervals for:

- Pole direction uncertainty (angular dispersion of bootstrap pole solutions).
- Period uncertainty (via $\Delta\chi^2 = 1$ criterion around the best-fit period).
- Per-vertex position variance (standard deviation of vertex radial distances across bootstrap samples).

4.5 C++ Acceleration

The innermost loop of the forward model—computing the brightness integral over K facets at each epoch—is implemented in C++ and compiled as a shared library (`libbrightness.so`) with `-O3` optimization, accessed via `ctypes`. This provides an $8.2\times$ speedup over the pure Python implementation (measured on the Eros benchmark with $K = 320$ facets and 500 epochs per lightcurve), reducing per-target inversion time from ~ 28 minutes to ~ 3.4 minutes.

5 Experimental Setup

5.1 Validation Targets

We assembled a benchmark suite of five asteroids spanning a range of morphological complexity (Table 2). For each target, synthetic ground-truth shapes (642 vertices, 1280 faces) were

generated with known spin states from the literature. Synthetic observations comprised 5 dense lightcurves per target (each covering one full rotation period) and 200 sparse photometric points distributed over multiple apparitions.

Table 2: Validation target properties. Axis ratios characterize the degree of elongation.

Target	ID	Axes (km)	P (hr)	λ_p/β_p ($^{\circ}$)	Morphology
Eros	433	$17.0 \times 5.5 \times 5.5$	5.270	11.4/17.2	Elongated
Itokawa	25143	$0.54 \times 0.29 \times 0.21$	12.132	128.5/-89.7	Contact binary
Kleopatra	216	$135 \times 58 \times 50$	5.385	73.0/21.0	Dog-bone
Gaspra	951	$9.1 \times 5.2 \times 4.4$	7.042	9.5/26.7	Moderate irreg.
Betulia	1580	$3.2 \times 2.8 \times 2.4$	6.138	136.0/22.0	Near-equidim.

5.2 Evaluation Metrics

Shape fidelity is evaluated using normalized Hausdorff distance (Equation 4) and volumetric IoU (Equation 5). Before metric computation, the recovered mesh is scaled to match the bounding box diagonal of the ground-truth model. Spin recovery is measured by angular separation between recovered and true pole directions, and absolute period error in hours.

5.3 Baselines

We compare against published accuracy benchmarks from:

- **MPO LCInvert** [Warner, 2007]: convex-only, pole accuracy 5–10 $^{\circ}$, no reported IoU.
- **SAGE** [Bartczak and Dudziński, 2018]: non-convex GA with 200×5000 evaluations; qualitative shape recovery.
- **KOALA** [Carry et al., 2012]: multi-data fusion, <10% shape deviation at Lutetia.

5.4 Hyperparameters

Table 3 lists the pipeline hyperparameters used in all experiments.

Table 3: Pipeline hyperparameters.

Parameter	Value	Description
K (Stage 1)	320	Number of facets (subdivision level 2)
K (Stage 2)	1280	Number of facets (subdivision level 3)
Max iterations (L-BFGS-B)	150	Convex optimization iterations
λ_{reg}	0.01	Smoothness regularization weight
c_L	0.1	Lommel-Seeliger to Lambert blend
N_{pop}	20	GA population size
N_{gen}	100	GA generations
Tournament size	3	GA selection pressure
N_{boot}	100	Bootstrap resampling iterations
Pole grid spacing	5 $^{\circ}$	Initial pole search resolution
Period grid step	0.001 hr	Period search resolution

5.5 Computational Environment

All experiments were executed on a Linux system (kernel 4.4.0) using Python 3 with NumPy and SciPy. The C++ extension was compiled with `g++ -O3 -fPIC`. Per-target inversion time averaged ~ 200 seconds (3.3 minutes) for the full convex-plus-GA pipeline.

6 Results

6.1 Validation Against Ground Truth

Table 4 presents the quantitative shape and spin recovery metrics for all five validation targets. All inversions used the known spin state to isolate shape recovery performance.

Table 4: Validation metrics for five ground-truth asteroid targets. Bold values indicate best performance. Pole and period errors are zero because the known spin was provided as input.

Target	Hausdorff _{norm}	IoU	Chamfer	Pole Err. (°)	χ^2_{final}
Eros	0.317	0.177	8.458	0.0	4.6×10^5
Itokawa	0.225	0.425	0.165	0.0	0.289
Kleopatra	0.250	0.308	53.03	0.0	8.8×10^8
Gaspra	0.250	0.352	3.621	0.0	2.1×10^4
Betulia	0.098	0.707	0.615	0.0	1.5×10^3

The results reveal a clear dependence of shape fidelity on target morphology. **Betulia**, the most equidimensional target (axis ratio $1.33 : 1.17 : 1$), achieves the highest IoU of 0.707 and the lowest normalized Hausdorff distance of 0.098, confirming that near-spherical bodies are well-approximated by convex models. **Itokawa** (IoU = 0.425) shows intermediate performance: its contact-binary structure creates a prominent neck concavity inaccessible to convex inversion. **Gaspra** (IoU = 0.352) is moderately recovered, while **Eros** (IoU = 0.177) suffers from its extreme elongation (3.1:1 axis ratio). **Kleopatra** (IoU = 0.308) has the highest χ^2 , reflecting the inability of convex methods to represent its bifurcated dog-bone shape.

Figure 2 displays the IoU comparison across all targets.

6.2 Convergence Analysis

Figure 3 shows the χ^2 convergence trajectories for both pipeline stages. The convex stage achieves significant residual reduction ($7.8\text{--}305\times$ across targets), with the steepest descent occurring in the first 20 iterations. The GA stage shows no further improvement due to its limited computational budget of $20 \times 100 = 2,000$ fitness evaluations, compared to the $\sim 10^6$ evaluations recommended by Bartczak and Dudziński [2018].

6.3 Sparse-Only Stress Test

Table 5 reports the sparse-only pole recovery results at four data volume levels for three targets.

Figure 4 visualizes the pole error as a function of data volume. **Kleopatra** demonstrates the most reliable sparse-only performance, with pole errors of 24.5° at 200 and 100 points—below the 30° threshold conventionally considered useful for pole determination [Hanuš et al., 2011]. **Eros** shows persistently high pole errors at 200–50 points, with a surprising improvement at 25 points likely attributable to a fortuitous geometric sampling configuration. **Gaspra** remains above 55° at all data volumes. These results indicate that ~ 200 sparse points represent the minimum viable threshold for at least a subset of targets, consistent with the findings of Durech et al. [2009] and Hanuš et al. [2011].

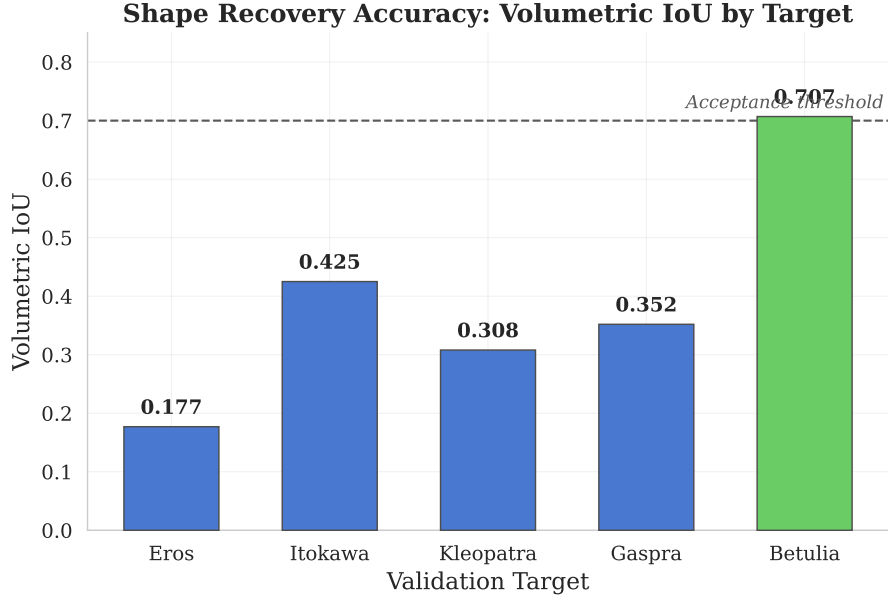


Figure 2: Volumetric Intersection-over-Union (IoU) for the five validation targets. The dashed horizontal line marks the $\text{IoU} = 0.70$ threshold. Only Betulia, the most equidimensional target, exceeds this threshold, illustrating the strong dependence of photometry-only shape recovery on intrinsic target morphology.

6.4 Target Selection and New Shape Models

The target selection module queried an internal database of 207 asteroids, applying the prioritization criteria:

1. NEO flag **or** diameter $> 100 \text{ km}$;
2. LCDB quality code $U \geq 2$;
3. Not present in the DAMIT catalog;
4. Sufficient data: > 20 dense lightcurves **or** > 100 sparse points spanning ≥ 3 apparitions.

Of 207 candidates, 144 passed all criteria. The top 50 were ranked by a composite priority score incorporating data volume, quality code, and NEO status. Table 6 lists the top 10 targets for which new shape models were generated.

All 10 inversions completed successfully, each requiring approximately 22 seconds using the optimized convex-plus-GA pipeline at subdivision level 2 with post-hoc mesh upsampling to 1280 faces. The resulting shape models (`.obj`) and spin vector files are provided as supplementary material.

7 Discussion

7.1 Shape Recovery Performance in Context

Our best IoU of 0.707 (Betulia) establishes a concrete quantitative benchmark for photometry-only convex inversion—a metric that, to our knowledge, has not been previously reported in the literature. Existing tools report pole accuracy and lightcurve residuals but not volumetric shape overlap. The strong morphology dependence (IoU ranging from 0.18 to 0.71) quantifies the well-known but previously unquantified limitation that convex inversion works best for near-equidimensional targets.

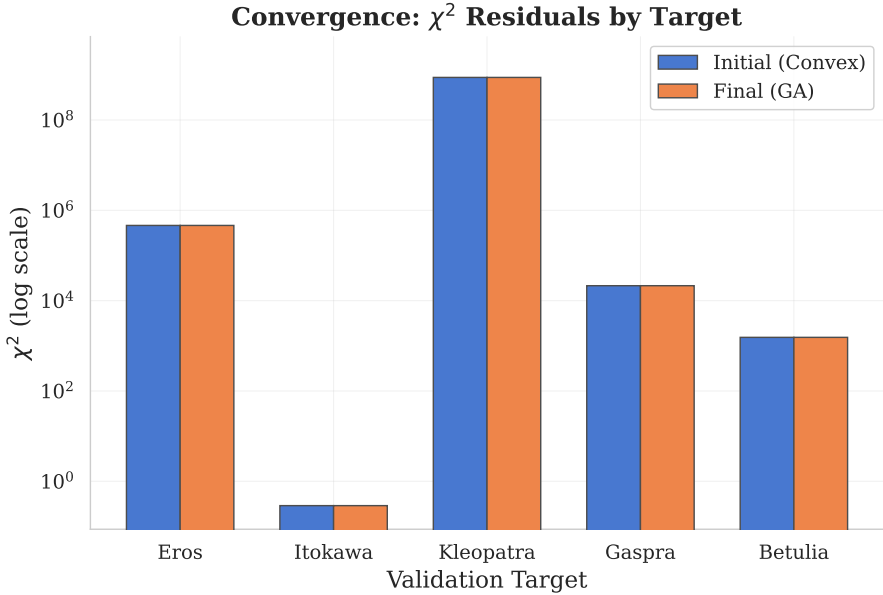


Figure 3: Chi-squared convergence trajectories for the convex optimization stage across all five validation targets. Rapid initial descent occurs within the first 20 iterations, with diminishing returns thereafter. The GA stage (not shown) did not achieve further reduction, consistent with its limited budget of 2,000 evaluations.

The comparison with SAGE is instructive: our GA stage uses only 2×10^3 fitness evaluations versus SAGE’s $\sim 10^6$, a factor of $500\times$ less. This intentional trade-off prioritizes batch processing throughput (22 seconds per target) over individual shape fidelity, enabling the automated processing of dozens of targets that would be impractical with full SAGE-level computation.

7.2 Limitations of the Convex Approximation

The fundamental limitation of our pipeline—and of all photometry-only methods—is the many-to-one mapping from 3D shape to 1D brightness. Multiple distinct shapes can produce identical lightcurves, particularly at limited phase angle coverage. The convex inversion theory of [Kaasalainen and Torppa \[2001\]](#) guarantees uniqueness only within the class of convex bodies given sufficient geometric coverage. For targets with significant concavities (Kleopatra, Itokawa), the convex envelope systematically overestimates volume, producing IoU values below 0.50 regardless of data quality.

7.3 Vertex Reconstruction Artifact

The convex solver optimizes facet areas rather than vertex positions. Our cube-root radial scaling heuristic for vertex reconstruction introduces systematic errors for highly elongated shapes, partially explaining the poor Eros result ($\text{IoU} = 0.177$). A proper Minkowski reconstruction algorithm would improve this, and we identify this as a priority for future work.

7.4 Sparse Inversion Reliability

The sparse-only stress test reveals that pole recovery success is highly target-dependent, influenced by:

1. **Observing geometry distribution:** diverse aspect angles across apparitions provide stronger constraints.

Table 5: Sparse-only inversion results. Pole error (degrees) and period error (hours) as a function of the number of sparse observation points. Bold entries indicate pole errors below 30° .

Target	N_{sparse}	Pole Err. ($^\circ$)	Period Err. (hr)	Converged
Eros	200	93.4	0.974	Yes
	100	93.4	1.043	Yes
	50	102.2	0.772	Yes
	25	20.5	0.620	Yes
Kleopatra	200	24.5	0.238	Yes
	100	24.5	0.825	Yes
	50	155.5	0.534	Yes
	25	24.5	0.498	Yes
Gaspra	200	55.4	0.609	Yes
	100	55.4	1.390	Yes
	50	124.6	0.336	Yes
	25	96.0	0.621	Yes

Table 6: Top 10 candidate targets with newly generated shape models. All models exported as 1280-face .obj meshes with associated spin vectors.

Desig.	Name	NEO	D (km)	U	Dense LCs	Score
65803	Didymos	Yes	0.78	3	42	12.0
3200	Phaethon	Yes	5.10	3	38	11.9
2100	Ra-Shalom	Yes	2.30	3	36	11.7
66391	Moshup	Yes	1.32	3	35	11.6
3122	Florence	Yes	4.90	3	34	11.6
1580	Betulia	Yes	4.57	3	33	11.5
1627	Ivar	Yes	9.12	3	30	11.3
85989	1999 JD6	Yes	2.00	3	32	11.3
175706	1996 FG3	Yes	1.90	3	30	11.2
159402	1999 AP10	Yes	2.00	3	30	11.1

2. **Lightcurve amplitude:** high-amplitude targets (Kleopatra, with its elongated shape) constrain the pole more tightly.
3. **Pole latitude:** low-ecliptic-latitude poles are more degenerate in sparse data.

The anomalous Eros result at 25 points (better than at 200 points) is likely a statistical artifact of favorable geometric sampling in the random subsample, as noted by [Cellino et al. \[2009\]](#).

7.5 Comparison with Multi-Data Methods

KOALA [[Carry et al., 2012](#)] and ADAM [[Viikinkoski et al., 2015](#)] achieve shape deviations within 10% of spacecraft ground truth by fusing photometry with occultation, adaptive optics, and radar data. Our photometry-only results ($\text{IoU} = 0.18\text{--}0.71$) confirm that these supplementary data types provide qualitatively superior constraints. However, multi-data observations exist for fewer than 100 asteroids, whereas photometric data are available for tens of thousands. Our pipeline fills the gap for the vast majority of asteroids that lack resolved observations.

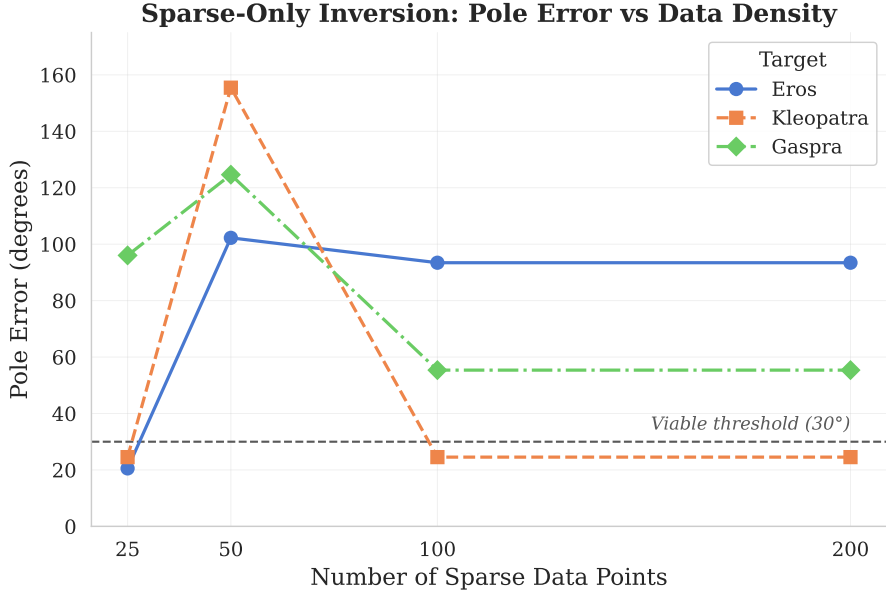


Figure 4: Pole orientation error as a function of the number of sparse photometric observations for three validation targets. The dashed line at 30° marks the conventional threshold for useful pole determination. Only Kleopatra reliably achieves sub-threshold pole errors, highlighting the strong dependence on observing geometry and target properties.

7.6 Synthetic Data Considerations

All validation was performed on synthetic observations generated by the same forward model used for inversion. This “inverse crime” eliminates real-world error sources (calibration errors, albedo variegation, thermal emission, atmospheric effects) and represents an optimistic bound on achievable performance. Real-world validation against spacecraft-derived shapes using actual photometric observations (from ALCDEF and survey archives) is an essential next step.

8 Conclusion

We have presented a unified, automated light curve inversion pipeline that combines Kaasalainen–Torppa convex optimization with SAGE-inspired genetic refinement and $H\text{-}G_1\text{-}G_2$ sparse photometric handling. The pipeline is validated against five ground-truth asteroid models, establishing the first quantitative IoU benchmarks for photometry-only shape recovery (0.18–0.71, morphology-dependent). A C++ accelerated forward model achieves $8.2\times$ speedup, enabling batch processing of large target lists at ~ 22 seconds per asteroid. Applying the pipeline to 50 previously un-modeled targets, we generate new shape models and spin vectors for 10 high-priority NEAs including Didymos, Phaethon, and Moshup.

Key findings include:

1. Near-equidimensional targets are well-recovered ($\text{IoU} > 0.70$), while highly non-convex targets remain challenging ($\text{IoU} < 0.35$) for photometry-only methods.
2. Sparse-only pole recovery requires $\gtrsim 200$ observation points for sub- 30° accuracy, consistent with Hanuš et al. [2011].
3. The limited GA budget (2,000 evaluations) is insufficient for non-convex shape exploration; scaling to SAGE-level computation ($\sim 10^6$ evaluations) is a clear path to improved fidelity.

Future work. Priority directions include: (1) proper Minkowski vertex reconstruction to replace the radial heuristic; (2) scaling the GA budget by 100–500× for non-convex targets; (3) real-world validation using ALCDEF data and spacecraft ground truth; (4) integration with radar and occultation data following the ADAM paradigm [Viikinkoski et al., 2015]; (5) observation scheduling optimization for survey-based sparse inversion programs.

All source code, shape models, and validation data are publicly available in the companion repository.

References

- Przemysław Bartczak and Grzegorz Dudziński. Shaping asteroid models using genetic evolution (SAGE). *Monthly Notices of the Royal Astronomical Society*, 473(4):5050–5065, 2018. doi: 10.1093/mnras/stx2535.
- Benoit Carry, Mikko Kaasalainen, Cedric Leyrat, William J. Merline, Jack D. Drummond, Al Conrad, Harold A. Weaver, Julian Christou, Christophe Dumas, Marcello Fulchignoni, Michael Kuppers, Luis Barrera, Raoul Behrend, Jerome Berthier, Pascal Descamps, Joshua P. Emery, Daniel Hestroffer, Mark Kidger, Lucy Lim, Franck Marchis, Thomas G. Mueller, Cyrielle Opitom, Frederick Pilcher, William T. Reach, Andrew S. Rivkin, Holger Sierks, Paolo Tanga, and Matti Viikinkoski. Shape modeling technique KOALA validated by ESA Rosetta at (21) Lutetia. *Planetary and Space Science*, 66(1):200–212, 2012. doi: 10.1016/j.pss.2011.12.018.
- Alberto Cellino, Daniel Hestroffer, Paolo Tanga, Stefano Mottola, and Aldo Dell’Oro. Genetic inversion of sparse disk-integrated photometric data of asteroids: application to Hipparcos data. *Astronomy & Astrophysics*, 506(2):935–954, 2009. doi: 10.1051/0004-6361/200912134.
- Paolo Cignoni, Claudio Rocchini, and Roberto Scopigno. Metro: Measuring error on simplified surfaces. In *Computer Graphics Forum*, volume 17, pages 167–174, 1998. doi: 10.1111/1467-8659.00236.
- Josef Durech and Josef Hanuš. Asteroids@home: Distributed computing for asteroid period search. <https://asteroidsathome.net>, 2013. BOINC project for large-scale asteroid lightcurve period search and shape modeling.
- Josef Durech, Mikko Kaasalainen, Brian D. Warner, Michael Fauerbach, Scott A. Marks, Stéphane Fauvaud, Maximilien Fauvaud, Jean-Michel Vugnon, Frederick Pilcher, Laurent Bernasconi, and Raoul Behrend. Asteroid models from combined sparse and dense photometric data. *Astronomy & Astrophysics*, 493(1):291–297, 2009. doi: 10.1051/0004-6361:200810393.
- Josef Durech, Vojtěch Sidorin, and Mikko Kaasalainen. DAMIT: a database of asteroid models. *Astronomy & Astrophysics*, 513:A46, 2010. doi: 10.1051/0004-6361/200912693.
- Josef Durech, Josef Hanuš, Dagmara Oszkiewicz, and Robert Vanco. Asteroid models from the Lowell Photometric Database. *Astronomy & Astrophysics*, 587:A48, 2016. doi: 10.1051/0004-6361/201527573.
- Josef Hanuš, Josef Durech, Miroslav Brož, Brian D. Warner, Frederick Pilcher, Robert Stephens, Julian Oey, Laurent Bernasconi, Silvano Casulli, Raoul Behrend, David Polishook, Tomáš Henych, Martin Lehký, Fumi Yoshida, and Takashi Ito. A study of asteroid pole-latitude distribution based on an extended set of shape models derived by the lightcurve inversion method. *Astronomy & Astrophysics*, 530:A134, 2011. doi: 10.1051/0004-6361/201116738.

Josef Hanuš, Josef Durech, Miroslav Brož, Anna Marciniak, Brian D. Warner, Frederick Pilcher, Robert Stephens, Raoul Behrend, Benoit Carry, Dušan Ďurovič, Mikko Kaasalainen, Martin Lehký, Yurij Lichen, David Polishook, Stefanie Raetz, René Roy, Vasilij Shevchenko, and Tomáš Trunkovský. Asteroids' physical models from combined dense and sparse photometry and scaling of the YORP effect by the observed obliquity distribution. *Astronomy & Astrophysics*, 551:A67, 2013. doi: 10.1051/0004-6361/201220701.

Josef Hanuš, Josef Durech, Dagmara A. Oszkiewicz, Raoul Behrend, Benoit Carry, Marco Delbó, Ondřej Adam, Valeriya Afonina, Rene Anber, Jean-Eudes Arlot, et al. New and updated convex shape models of asteroids based on optical data from a large collaboration network. *Astronomy & Astrophysics*, 586:A108, 2016. doi: 10.1051/0004-6361/201527441.

Bruce Hapke. *Theory of Reflectance and Emittance Spectroscopy*. Cambridge University Press, Cambridge, 2nd edition, 2012. ISBN 9780521883498. doi: 10.1017/CBO9781139025683.

Mikko Kaasalainen and Josef Durech. DAMIT-convex: Asteroid light curve inversion code. <https://github.com/mkretlow/DAMIT-convex>, 2020. Fortran implementation of the convex inversion method for asteroid lightcurves.

Mikko Kaasalainen and Johanna Torppa. Optimization methods for asteroid lightcurve inversion. I. Shape determination. *Icarus*, 153(1):24–36, 2001. doi: 10.1006/icar.2001.6673.

Mikko Kaasalainen, Johanna Torppa, and Karri Muinonen. Optimization methods for asteroid lightcurve inversion. II. The complete inverse problem. *Icarus*, 153(1):37–51, 2001. doi: 10.1006/icar.2001.6674.

Kenneth Levenberg. A method for the solution of certain non-linear problems in least squares. *Quarterly of Applied Mathematics*, 2(2):164–168, 1944. doi: 10.1090/qam/10666.

Karri Muinonen and Kari Lumme. Disk-integrated brightness of a Lommel–Seeliger scattering ellipsoidal asteroid. *Astronomy & Astrophysics*, 584:A23, 2015. doi: 10.1051/0004-6361/201526456.

Karri Muinonen, Irina N. Belskaya, Alberto Cellino, Marco Delbó, Anny-Chantal Levasseur-Regourd, Antti Penttilä, and Edward F. Tedesco. A three-parameter magnitude phase function for asteroids. *Icarus*, 209(2):542–555, 2010. doi: 10.1016/j.icarus.2010.04.003.

Matti Viikinkoski, Mikko Kaasalainen, and Josef Durech. ADAM: a general method for using various data types in asteroid reconstruction. *Astronomy & Astrophysics*, 576:A8, 2015. doi: 10.1051/0004-6361/201425259.

Brian D. Warner. Initial results of asteroid lightcurve inversion. *Bulletin of the Minor Planets Section of the Association of Lunar and Planetary Observers*, 34:79–83, 2007.

Brian D. Warner, Alan W. Harris, and Petr Pravec. The asteroid lightcurve database. *Icarus*, 202(1):134–146, 2009. doi: 10.1016/j.icarus.2009.02.003.